International Journal of Computer Assisted Radiology and Surgery (2019) 14:671–683
https://doi.org/10.1007/s11548-018-01906-w

ORIGINAL ARTICLE

A novel robotic system for vascular intervention: principles, performances, and applications

Hao Shen[1] · **Cheng Wang**[2] · **Le Xie**[1,3] · **Shoujun Zhou**[2] · **Lixu Gu**[3] · **Hongzhi Xie**[4]

Received: 4 July 2018 / Accepted: 26 December 2018 / Published online: 9 February 2019

Abstract

Purpose This paper describes the design, principles, performances, and applications of a novel image-guided master–slave robotic system for vascular intervention (VI), including the performance evaluation and in vivo trials.

Methods Based on the peer-to-peer (P2P) remote communication system, the kinetics analysis, the sliding-mode neural network self-adaptive control model and the feedback system, this new robotic system can accomplish in real time a number of VI operations, including guidewire translation and rotation, balloon catheter translation, and contrast agent injection. The master–slave design prevents surgeons from being exposed to X-ray radiation, which means that they are not required to wear a heavy lead suit. We also conducted a performance evaluation of the new system, which assessed the speed, position tracking, and accuracy, as well as in vivo swine trials.

Results The speed and position tracking effects are really good, which contribute to the high level of performance in terms of the translational (error $\leq 0.45\%$) and rotational (error $\leq 2.6°$) accuracy. In addition, the accuracy of the contrast agent injection is less than 0.2 ml. The robotic system successfully performed both the stent revascularization of an arteria carotis and four in vivo trials. The haptic feedback data correspond with the robotic-assisted procedure, and peaks and troughs of data occur regularly.

Conclusions By means of the performance evaluation and four successful in vivo trials, the feasibility and efficiency of the new robotic system are validated, which should prove helpful for further research.

Keywords VI robotic system · Kinetics · Sliding-mode neural network · Haptic feedback · Performance evaluation · In vivo swine trial

Introduction

Vascular diseases affect millions of people worldwide, with an estimated 18.0 million deaths having occurred due to cardiovascular disease in 2015 alone [1, 2]. Vascular intervention (VI) is considered to be a minimally invasive approach for the treatment of such diseases. However, conventional VI has a number of limitations. First, both the patient and medical staff are exposed to high doses of X-ray radiation during the procedure. Second, navigating through the complex network of tiny vessels is highly challenging and hence likely to lead to errors. Third, surgeons often become fatigued due to having to wear a heavy lead suit in order to mitigate their radiation exposure. The emergence of VI robots could serve to address all these issues.

In recent years, numerous studies have been conducted in relation to VI robotic systems [3–6]. Worldwide, there are mainly three driving methods used in the robotic system. One is known as the progressive driving method [7]. According to this method, the actuator advances the catheter or guidewire step by step using the clamps. The second method is known as the friction-wheel driving method [8–15]. It

---

Hao Shen and Cheng Wang have contributed equally to this paper.

✉ Le Xie
lexie@sjtu.edu.cn

✉ Shoujun Zhou
sj.zhou@siat.ac.cn

[1] Institute of Forming Technology and Equipment, Shanghai Jiao Tong University, Building Med-X, No. 1954, Huashan Road, Xuhui District, Shanghai, China

[2] Shenzhen Institutes of Advanced Technology, Chinese Academy of Sciences, Beijing, China

[3] School of Biomedical Engineering, Shanghai Jiao Tong University, Xuhui, China

[4] Peking Union Medical College Hospital, Beijing, China

involves the actuator using friction wheels to advance the catheter or guidewire by means of the generated friction. The third method is known as the continuous driving method [16]. It involves the actuator advancing the catheter or guidewire along a long pathway in a single step. For all three methods, the real-time image guide and remote communication system are of vital importance in the robotic system. In the case of real VI, the surgeon performs the operation so as to advance the guidewire or catheter into the target vessel based on the fluoroscopy image guide. Due to questions about the safety of the robotic-assisted procedure, the real-time performance of the remote communication system is a matter of great concern. Additionally, the haptic feedback information involved in real VI is considered so vital that a haptic feedback function is also deemed necessary in robotic system.

Based on the requirements of VI [17], we developed a real-time image-guided master–slave robotic system (Fig. 1) (for more detailed information, please refer to [18]) to perform VI. The main driving module of the robotic system looks like the Hansen Medical robot [12], but the driving principle is different. Our robotic system avoids the disadvantages and takes advantage of the progressive driving method, friction-wheel driving method, and continuous driving method. The Hansen uses the friction-wheel driving method. Moreover, Hansen just focuses on the guiding catheter driving. Our robotic system can accomplish the guidewire translation and rotation, balloon catheter translation, and contrast agent injection. Following the first successful in vivo trial, we performed a comprehensive optimization based on the identified problems. A model test was conducted to evaluate the master–slave control accuracy of the robotic system. Moreover, an in vivo trial was conducted to mimic the partial procedures involved in the stent revascularization of an arteria carotis.

Materials and methods

During robotic-assisted VI, surgeons operate a master device (Omega 3) located at a safe distance from the ionizing radiation source to control a slave device tasked with advancing, retracting, and rotating interventional instruments using both real-time image guidance and haptic feedback. The peer-to-peer (P2P) remote communication system allows the real-time transmission of feedback information, such as the translational and rotational speed and position, fluoroscopy images, and haptic feedback data. Figure 2 illustrates the process behind robotic-assisted VI.

The control architecture

Figure 3 presents the control architecture of the VI robotic system. The surgeon's side is the master side, while the patient's side is the slave side. The first step in the robotic-assisted VI procedure is to locate the actuator, which aims to situate the actuator as close as possible to the puncture position. A customized robotic arm (three rotational and one translational degrees of freedom [DoFs]) is used to locate the actuator, which is controlled by a haptic device, namely the Omega 3. During the robotic-assisted VI procedure, the surgeon operates the Omega 3 to control the actuator. Under the surgeon's control, the actuator can perform guidewire translation and rotation, balloon catheter translation, and contrast agent injection. The injection speed and volume of the contrast agent are directly inputted on the screen by the surgeons. Based on the P2P distributed system, the control instructions are transmitted in real time to the patient's side via the local area network (LAN). On the patient's side, an ultrasonic sensor (manufacturer FGHGF, model: HC-SR04) captures position information in real time, while a force/torque sensor captures force/torque information. The real-time position feedback information monitors the movement of the shifting board. (It was mentioned in [18].) The real-time haptic feedback information reflects the guidewire's situation within the blood vessels. The position information and haptic feedback information are transmitted in real time to the surgeon's side via the P2P remote communication system [19]. The display center shows the real-time fluoroscopy image, feedback information, and control instructions. By following the guidance provided by the real-time fluoroscopy image and feedback information, the surgeons can perform a more accurate and effective operation.

Kinetics analysis and sliding-mode neural network self-adaptive control of the actuator

The robustness of the robotic system determines its stability and safety. Therefore, the dynamic control of the robotic system is particularly important. We hence needed to elucidate the kinetic model of the actuator and formulate the corresponding control strategy.

Due to the design of the actuator (for further details, please refer to [18]), the energy relations of each module of the actuator involve mutual independence and non-interference. Therefore, it is necessary to discuss the kinetic model of each module separately. Figure 4 shows the kinetic model of the guidewire rotation module, where θ is the angular displacement of the motor, $\dot{\theta}$ is the angular velocity, $\ddot{\theta}$ is the angular acceleration, $\dot{\theta}'$ and $\ddot{\theta}'$ are the angular velocity and acceleration, respectively, of the gear 4, I_i is the moment of inertia of the components, F_b is the viscous friction coefficient between the rotation axis and the bearings, $\mathrm{T}_s(\dot{\theta})$ is the torque of fastening and loosening the chuck related to $\dot{\theta}$, T_i

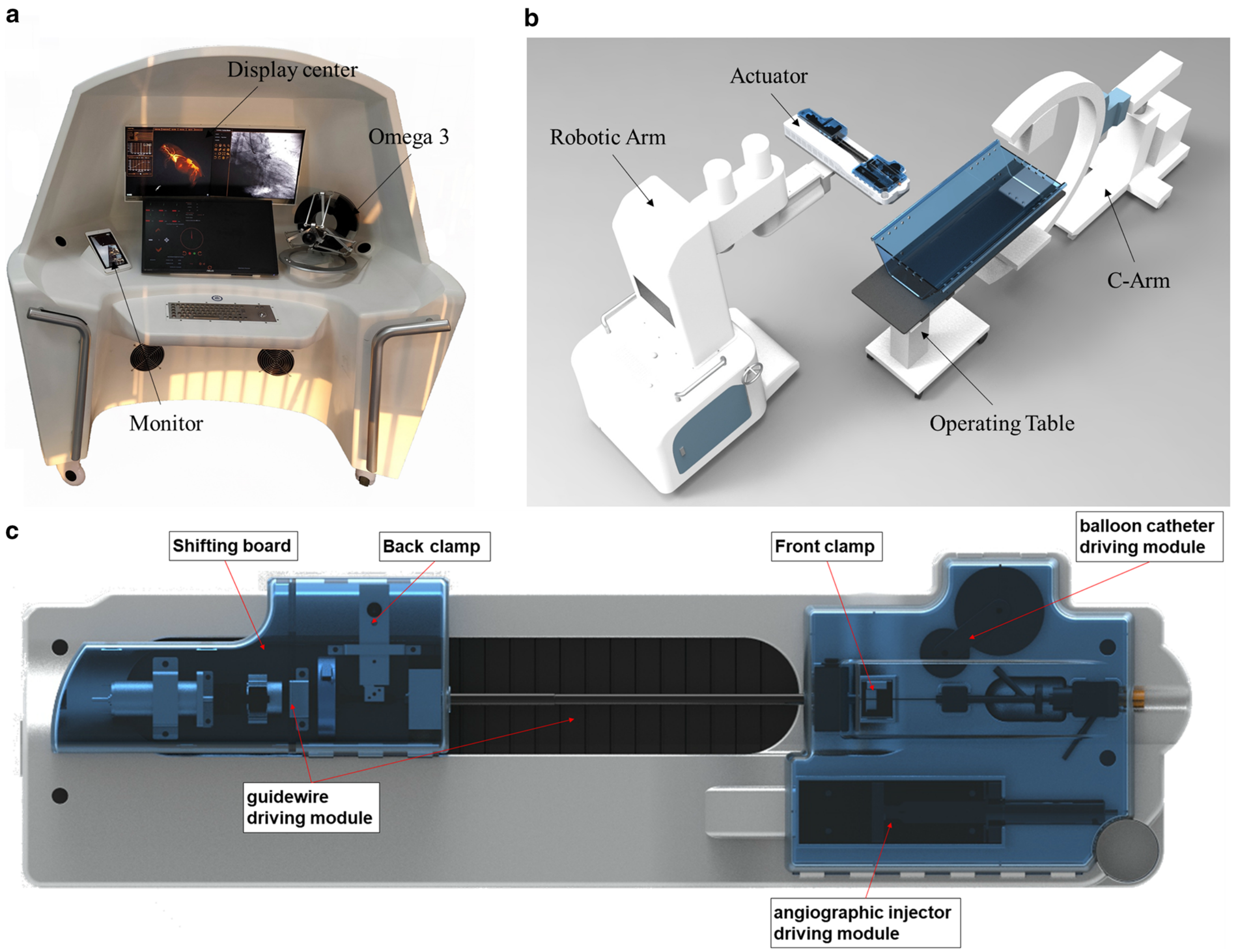

Fig. 1 **a** Master console platform; **b** patient side, **c** actuator

is the torque feedback given by the guidewire. Based on the Lagrange formulation [20–22]

$$\begin{cases} \frac{d}{dt}\left(\frac{\partial \mathcal{L}}{\partial \dot{q}}\right)^T - \left(\frac{\partial \mathcal{L}}{\partial q}\right)^T = \xi \\ \mathcal{L} = \mathcal{T} - \mathcal{U} \end{cases} \tag{1}$$

we discuss the kinematic model.

Based on the gear 4 and 5 meshing transmission relation, we can get:

$$\dot{\theta}' = \dot{\theta} \cdot \frac{R_5}{R_4} = k \cdot \dot{\theta} \tag{2}$$

According to the kinematic model, kinetic energy of the module is:

$$\mathcal{T} \approx \frac{1}{2}\dot{\theta}'^2 \cdot \sum_{i=1}^{4} I_i + \frac{1}{2}\dot{\theta}^2 \cdot (I_5 + I_6) = \frac{1}{2}k^2\dot{\theta}^2 \cdot \sum_{i=1}^{4} I_i + \frac{1}{2}\dot{\theta}^2 \cdot (I_5 + I_6) \tag{3}$$

According to the relationship between moment of inertia and mass, moment of inertia of each component is:

$$I_i = \int R_i^2 \mathrm{d}m_i \tag{4}$$

There is no potential change in the module, so we can get:

$$\mathcal{U} = 0 \tag{5}$$

Together with Eqs. (1), (3), (5), we can get the following result:

$$\mathcal{L} = \frac{1}{2}k^2\dot{\theta}^2 \cdot \sum_{i=1}^{4} I_i + \frac{1}{2}\dot{\theta}^2 \cdot (I_5 + I_6) \tag{6}$$

$$\frac{d}{dt}\frac{\partial \mathcal{L}}{\partial \dot{\theta}} - \frac{\partial \mathcal{L}}{\partial \theta} = k^2\ddot{\theta} \cdot \sum_{i=1}^{4} I_i + \ddot{\theta} \cdot (I_5 + I_6) \tag{7}$$

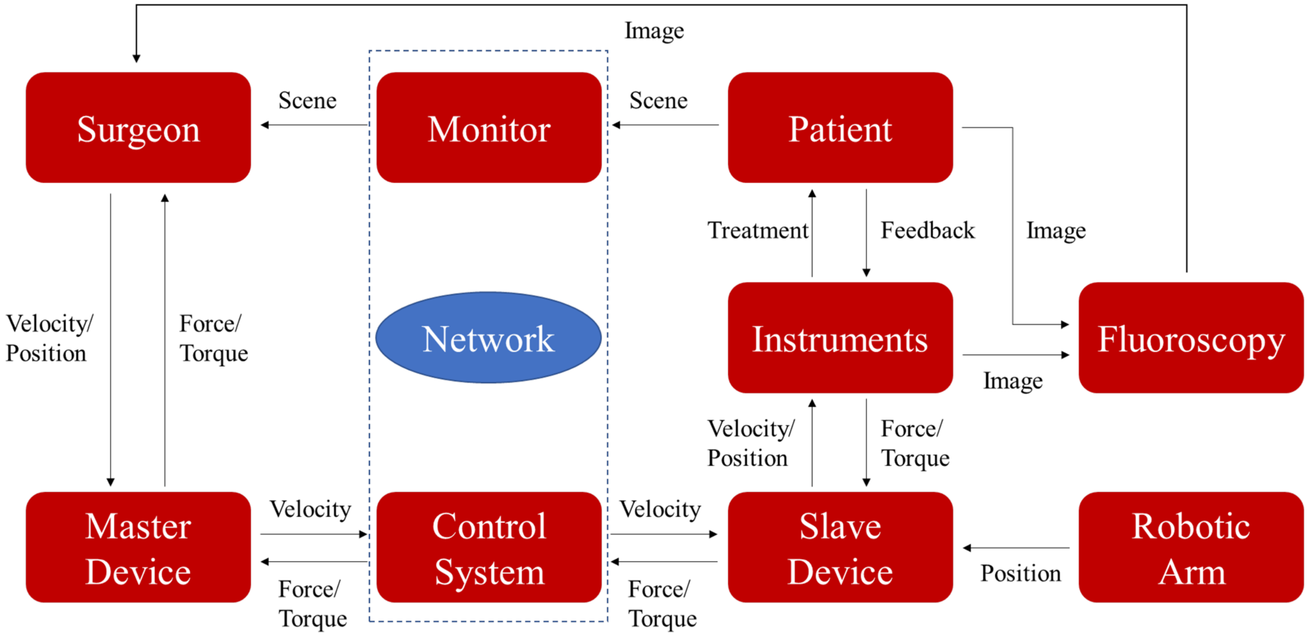

Fig. 2 Sketch of the robotic-assisted VI

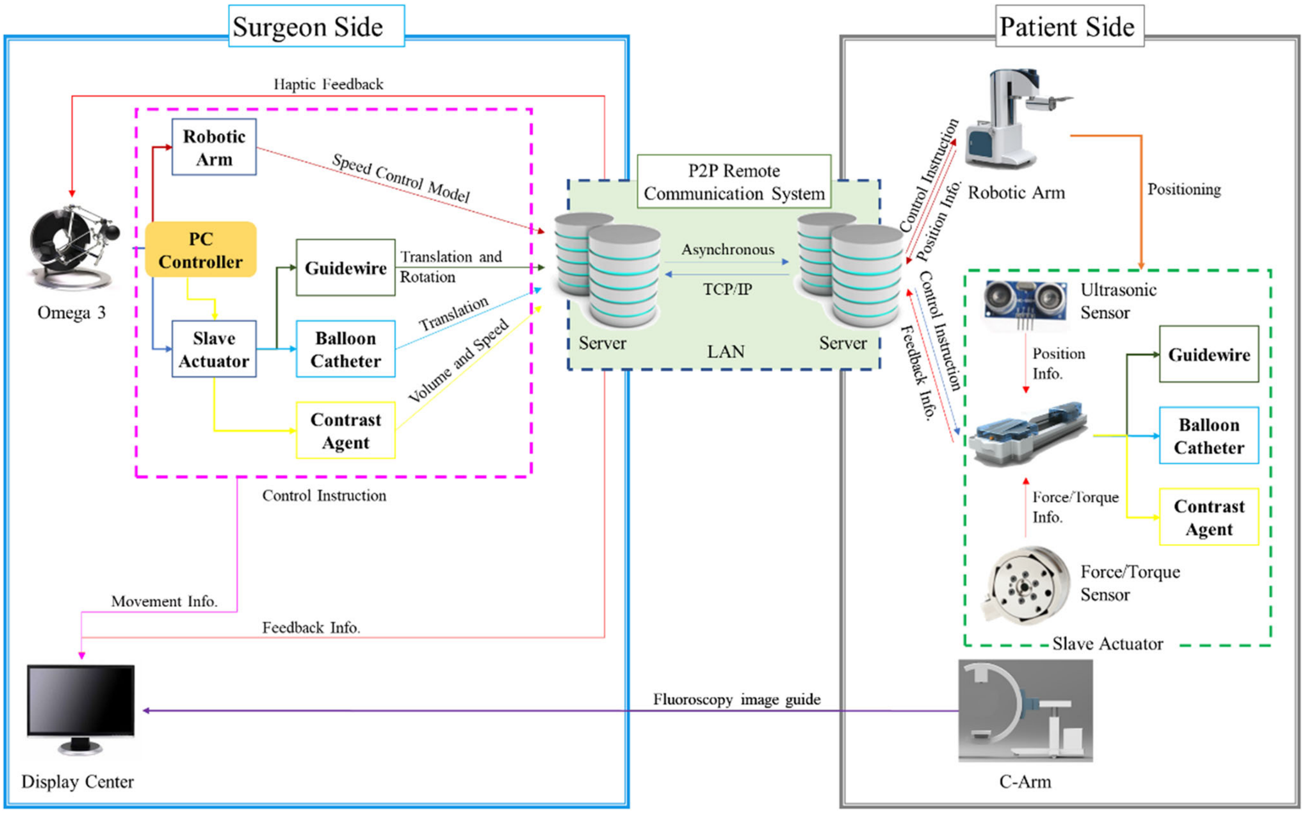

Fig. 3 Control architecture of the VI robotic system

The external force (torque) $\boldsymbol{\xi}$ is:

$$\xi = T_M - T_i - T_s\left(\dot{\theta}\right) - F_b \cdot \dot{\theta} \tag{8}$$

The kinetic equation of the rotation module is as follows:

$$k^2\ddot{\theta} \cdot \sum_{(i=1)}^{4} I_i + \ddot{\theta} \cdot (I_5 + I_6) + F_b \cdot \ddot{\theta} + T_s(\ddot{\theta}) + T_i = T_M \tag{9}$$

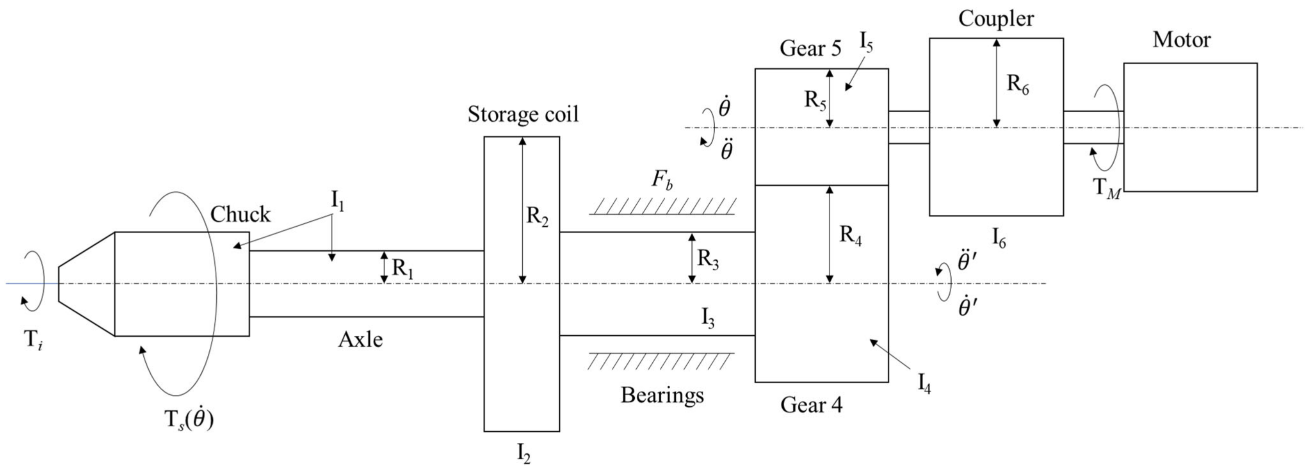

Fig. 4 Kinetic model of guidewire rotation module

Based on Eq. (9), it is possible to determine that the system is a nonlinear system and, further, that the direct relation between $T_s(\dot{\theta})$ and $\dot{\theta}$ cannot be explicitly calculated. In addition, T_i is a dynamic phase. The sliding mode control [23–25] is a nonlinear control, which matches the output to the desired input by changing the structure of the controlled object. This can overcome the uncertainty of the system, and it exhibits strong robustness in relation to interference and unmodeled dynamics, especially for the control of a nonlinear system. Given the characteristics of the kinetic model of the rotation module, a sliding mode control is suitable for the kinetic model. However, larger modeling uncertainties require a larger switch gain, which will cause chattering. A sliding mode control, when combined with the neural network approach to the implementation model of an unknown part of the adaptive approximation, effectively reduces the fuzzy gain [26, 27]. Moreover, when compared with a multilayer feed-forward back-propagation (BP) neural network, a radial basis function (RBF) neural network exhibits good generalization ability. The relatively simple neural network structure can help avoiding unnecessary and lengthy calculation. Therefore, we designed a sliding-mode neural network self-adaptive controller.

Based on the state equation of sliding mode control [26], we set $x_1 = \theta$, $x_2 = \dot{\theta}$,

$$f(x) = -\frac{1}{k^2\sum_{i=1}^{4} I_i + I_5 + I_6}\left(F_b \cdot x_2 + T_s(x_2)\right) \tag{10}$$

$$u = \frac{T_M}{k^2\sum_{i=1}^{4} I_i + I_5 + I_6} = \frac{A \cdot i_M}{k^2\sum_{i=1}^{4} I_i + I_5 + I_6} \tag{11}$$

and u is the desired input value, A is a relation coefficient of motor's torque and current i_M is the controlled current.

Set $x = \begin{bmatrix} x_1 & x_2 \end{bmatrix}^T$, and the output of the neural network is:

$$\hat{f}(x) = \hat{W}^{*T} h(x) \tag{12}$$

$$f(x) - \hat{f}(x) = W^{*T} h(x) + \varepsilon - \hat{W}^{*T} h(x) = -\tilde{W}^{*T} h(x) + \varepsilon \tag{13}$$

where x is the input of the neural network, $h = \left[h_j\right]^T$ is the Gauss function output of the neural network, j is the j node of the network hidden layer, W^* is the ideal weight of the neural network, ε is the approximation error.

Define the Lyapunov function:

$$V = \frac{1}{2}s^2 + \frac{1}{2\gamma}\tilde{W}^T\tilde{W} \tag{14}$$

and we get:

$$\dot{V} = s\dot{s} + \frac{1}{\gamma}\tilde{W}^T\dot{\hat{W}} = s(c(x_2 - \dot{x}_d) + f(x) + u - \ddot{x}_d) + \frac{1}{\gamma}\tilde{W}^T\dot{\hat{W}} \tag{15}$$

The design control law is:

$$u = -c(x_2 - \dot{x}_d) - \hat{f}(x) + \ddot{x}_d - \eta\,\mathrm{sgn}(s) \tag{16}$$

Together with Eqs. (15), (16), we can get:

$$\dot{V} = \varepsilon s - \eta|s| + \tilde{W}^T\left(\frac{1}{\gamma}\dot{\hat{W}} - h(x) \cdot s\right) \tag{17}$$

when $\eta > |\varepsilon|_{\max}$, $\dot{V} \leq 0$, and the adaptive control law is as follows:

$$\dot{\hat{W}} = \gamma h(x) \cdot s \tag{18}$$

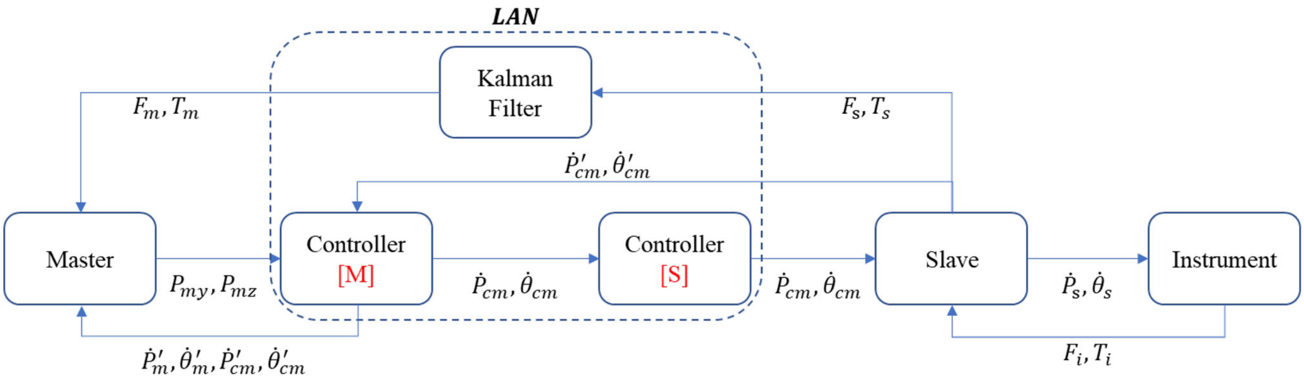

Fig. 5 Sketch of the haptic and velocity feedback

The above is the control strategy of the rotation module, and the other modules are similar to this module. The performance will be described in performance evaluation.

Feedback system

The feedback system of the robotic system involves haptic feedback, velocity feedback, and image feedback. The image feedback provides intuitive visual images for the surgeon to guide his operation. Figure 5 presents a sketch of the haptic and velocity feedback. The controllers [M] and [S] are used to receive and process the signals from the master and slave devices, respectively. P, $\dot{P}$, $\dot{\theta}$, F, T, and $f()$ are the position, linear velocity, angular velocity, force, torque, and method, respectively.

Through simple comparative experiments and the controller [M] processing, the influences of the friction (F_f, T_f) can be eliminated and $[F_m, T_m] = f_H([F_s, T_s])$. f_H is a haptic feedback model.

$$\left[\dot{P}_{cm}, \dot{\theta}_{cm}\right] = f_v\left(\left[P_{my}, P_{mz}, F_s, T_s\right]\right) \tag{19}$$

$$\left[\dot{P}_s, \dot{\theta}_s\right] = f_{io}\left(\left[\dot{P}_{cm}, \dot{\theta}_{cm}\right]\right) \tag{20}$$

$$\left[\delta_{\dot{P}}, \delta_{\dot{\theta}}\right] = \frac{\left[\dot{P}'_{cm}, \dot{\theta}'_{cm}\right]}{\left[\dot{P}_{cm}, \dot{\theta}_{cm}\right]} \times 100\% \tag{21}$$

where fv is a velocity control model, f_{io} is the relationship between input and output velocities, $\left[\delta_{\dot{P}}, \delta_{\dot{\theta}}\right]$ is the velocity accuracy.

Due to the measurement signal jitter of the transducer, high-frequency and low-amplitude vibrations (noisy signal) of the measurement results occur. This meaningless noisy signal distorts the useful signal, meaning that the useful signal is unable to demodulate. A Kalman filter [28–30] (f_H) is hence used for noise processing. The filter can be divided into two main parts, namely the priori estimation (time update) and the posteriori estimation (measurement update). The priori estimation can be summarized as follows:

$$\hat{x}_k^- = A\hat{x}_{k-1} + Bu_k \tag{22}$$

$$\hat{P}_k^- = A\hat{P}_{k-1}A^T + Q \tag{23}$$

The posteriori estimation can be summarized as follows:

$$K_k = \hat{P}_k^- H^T \left(H\hat{P}_k^- H^T + R\right)^{-1} \tag{24}$$

$$\hat{x}_k = \hat{x}_k^- + K_k\left(z_k - H\hat{x}_k^-\right) \tag{25}$$

$$\hat{P}_k = (1 - K_k H)\hat{P}_k^- \tag{26}$$

where $\hat{x}_k^-$ and $\hat{x}_{k-1}$ are the current priori estimation and previous *final* optimal estimation, respectively, u_k is the control input, $\hat{P}_k^-$ and $\hat{P}_{k-1}$ are the current priori estimation error covariance and previous *final* estimation error covariance, respectively, Q is the process noise covariance, K_k is the Kalman gain, R is the measurement noise covariance, $\hat{x}_k$ is the *final* optimal estimation, $\hat{P}_k$ is the *final* estimation error covariance, z_k is the measurement value (F, T), and A, B, H are the coefficient matrix, respectively.

The posteriori estimation, when combined with the current measurement, performs the predictive correction and obtains the *final* optimal estimation. In addition, given that surgeons rely on large variations in large values to guide the operation, while the Kalman filter significantly decreases those values, we added a threshold to the haptic feedback model. If the measurement value is bigger than the threshold, the Kalman filter will not work.

f_v is a velocity control model. The output velocity $\dot{P}_{cm}, \dot{\theta}_{cm}$ is determined by the input position P_{my}, P_{mz} of the Omega 3 and the real-time haptic feedback F_s, T_s. The velocity control model f_v can be divided into the position–velocity relation mapping model f_{vm} (for further details, please refer to [18]), and the haptic feedback safety strategy f_{vh}:

$$f_v\left(\left[\dot{P}_m, \dot{\theta}_m, F_s, T_s\right]\right) = f_{vm}\left(\left[P_{my}, P_{mz}\right]\right) \tilde{+} f_{vh}([F_s, T_s]) \tag{27}$$

f_{vh} aims to ensure surgical safety. When the values of the real-time haptic feedback F_s, T_s are bigger than the thresholds, that is, the safety values, the actuator withdraws the guidewire at a preset speed until the values of the real-time haptic feedback F_s, T_s decrease to lower than the thresholds. In summary, feedback system provides the information that is of crucial importance for the surgeon, since it helps to increase both the safety and the success of the robotic VI.

Performance evaluation

In order to test whether the robotic system meets the requirements, a primary performance evaluation was conducted. First, we evaluated the speed tracking of the motors. We set a required speed (translational speed = 400 rpm, rotational speed = 60 rpm) and a set acceleration (1000 rpm/s) for the driving motors. Converting the translational and rotational speeds of the driving motors into the advancement and rotation speeds of the guidewire resulted in 33.33 mm/s and 180 °/s, respectively. Based on the recommendation of an experienced physician (it takes 30 s to insert 90 cm length of the guidewire, if there is no obstacle), the maximum advancement speed of the guidewire was considered to be around 30 mm/s and the rotation speed to be very slow. We performed a MATLAB simulation of this sliding-mode neural network self-adaptive control model and thereby captured the actual moving speed (sampling frequency 50 frame/s). Moreover, to measure the translational and rotational accuracy, the actuator clamped a steel bar (diameter 2 mm) moving instead of a guidewire. The translational accuracy evaluation determined that the actuator advanced the steel bar at the set distances $d =$ 20.00, 30.00, 40.00, 50.00, and 60.00 mm. At the beginning of the advancement, the steel bar was marked and the distance $d1$ between the tip of the slave actuator and the marker was measured. After completing the advancement, the distance $d2$ between the tip of the slave actuator and the marker was measured again. The actual advancement distance can be determined as ($d2$–$d1$). The rotational precision evaluation determined that the actuator rotated the steel bar at the set angles $\vartheta = 15.0, 30.0, 45.0, 60.0$, and 75.0°. At the beginning of the rotation, a needle was fixed to the steel bar and the degree $\vartheta 1$ between the needle and the horizontal plane was measured. After completing the rotation, the degree $\vartheta 2$ was measured again. The actual rotation degree can be determined as ($\vartheta 2 - \vartheta 1$). The absolute error can be given as $|(\vartheta 2 - \vartheta 1) - \vartheta|$. The contrast agent dose was calibrated. The controller sets a series of injection volumes $V0 = 2.0$, 4.0, 6.0, 8.0, and 10.0 ml. We measured the volumes before and after the injection $V1$ and $V2$. Every set value calibration was tested five times.

Animal experiment

We used the designed robotic system for the stent revascularization [31] of an arteria carotis in an in vivo test. The protocol was approved by the Institutional Animal Care and Use Committee (Approval Number: S-20,171,016-01). A stent revascularization represents an effective treatment for carotid stenosis. We performed the entire procedure for the stent revascularization, using the robotic system to conduct the key procedures: angiography, guidewire insertion, and balloon catheter insertion. The in vivo trial was divided into seven steps, namely preoperative path planning, vascular puncture, manual guiding catheter and guidewire insertion, vascular angiography, automatic (robotic control) robotic-assisted guidewire insertion and balloon catheter insertion, remote-controlled (manual control) robotic-assisted guidewire insertion and balloon catheter insertion, and balloon inflation. Based on a previous magnetic resonance imaging (MRI) performed on the experimental swine (weight 28 kg, body length 89 cm), the surgeon determined the intervention path and chose the most appropriate interventional instruments (5French [5F] introducer sheath, 5F guiding catheter, 0.3-mm guidewire, 2.5-mm balloon catheter, 320 mg/ml nonionic iodixanol contrast agent). The surgeon chose the right arteria femoralis as the vascular puncture point. After placing the guiding catheter on the arteria carotis, the surgeon used the robotic system for remote angiography to observe the shape of the vascular network at the arteria carotis. Based on the angiographic result, the actuator automatically advanced the guidewire and the balloon catheter successively toward the guiding catheter tip. Afterward, the surgeon operated the Omega 3 so as to control the actuator advancing the guidewire and the balloon catheter successively to the target location in the arteria carotis. Finally, the surgeon used a pressure pump to inflate the balloon. During the procedure for the stent revascularization, the time, fluoroscopy images, and haptic feedback information were all recorded. When including previous trials, four trials have now been conducted. The four trials were performed by the same surgeon, and the vascular networks of the three experimental swine (the first two trials were performed on the same swine, while the other two trials were performed on different swines) were almost the same.

Results

Figure 6 shows the expected, simulation, and actual speed and position tracking curves of the guidewire driving module.

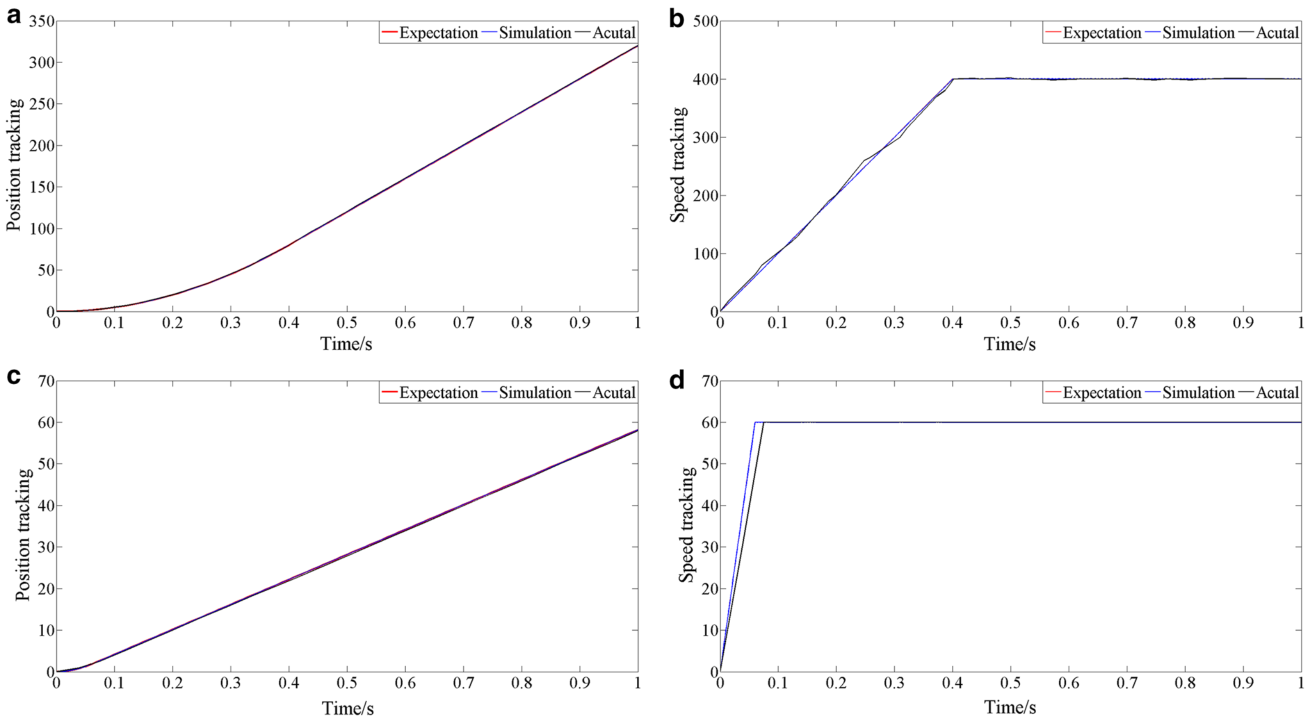

Fig. 6 Expected, simulation, and actual speed and position tracking curves of guidewire driving module

Table 1 Accuracy evaluation results of the robotic system

Item	Set value	Actual value (mean)	MD error	SD error	P value
Translation (mm)	20.00	19.91	0.45%	0.034	0.005
	30.00	29.88	0.40%	0.044	0.004
	40.00	40.13	0.33%	0.031	0.001
	50.00	50.05	0.10%	0.029	0.019
	60.00	59.95	0.08%	0.029	0.023
Rotation (°)	15.0	13.7	1.3°	0.36	0.001
	30.0	32.6	2.6°	0.36	<0.001
	45.0	44.0	1.0°	0.29	0.002
	60.0	61.5	1.5°	0.59	0.005
	75.0	76.0	1.0°	0.43	0.006
Injection (ml)	2.0	2.0	0.0 ml	0.089	0.374
	4.0	4.0	0.0 ml	0.089	0.374
	6.0	5.8	0.2 ml	0.089	0.016
	8.0	7.8	0.2 ml	0.14	0.034
	10.0	9.8	0.2 ml	0.17	0.033

Figure 6a, b shows the expected, simulation, and actual speed and position tracking curves of the guidewire translation module, while Fig. 6c, d shows the expected, simulation, and actual speed and position tracking curves of the guidewire rotation module. We also performed a data analysis of the evaluation results (T test confidence interval = 95%). Table 1 presents the analysis results concerning the robotic system. The P values of the translation and rotation evaluation results are all smaller than 0.005, which indicates that there was no significant difference between the control and experimental groups. Therefore, the evaluation results are effective. Although the P values of the 2 ml and 4 ml injection evaluation results are bigger than 0.005, the mean deviation (MD) errors are very small. An error of just 0.2 ml in relation to the contrast agent makes only a very small difference to the surgery.

The stent revascularization in vivo trial was successfully conducted without any angiorrhexis. Figure 7a–c shows

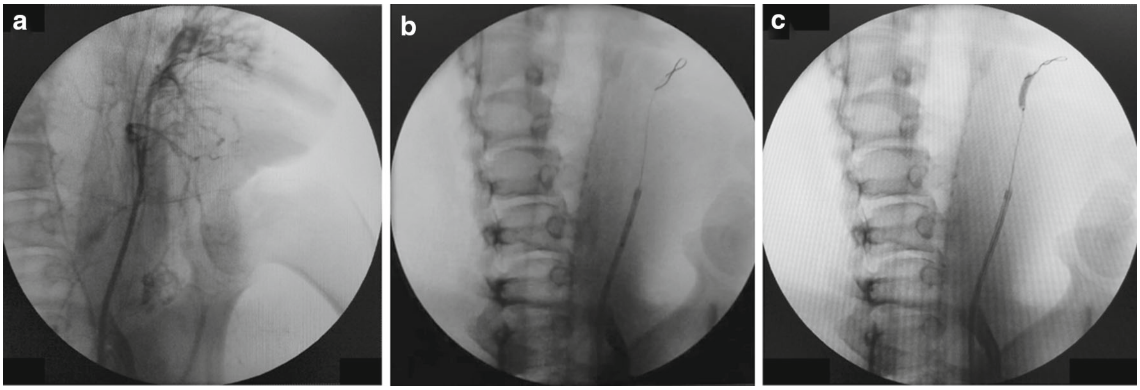

Fig. 7 Fluoroscopy images of stent revascularization in vivo trial: **a** angiography result; **b** robotic-assisted guidewire insertion result; **c** robotic-assisted balloon catheter insertion and inflation result

Fig. 8 Angiography and robotic-assisted guidewire insertion results of second and third in vivo trials

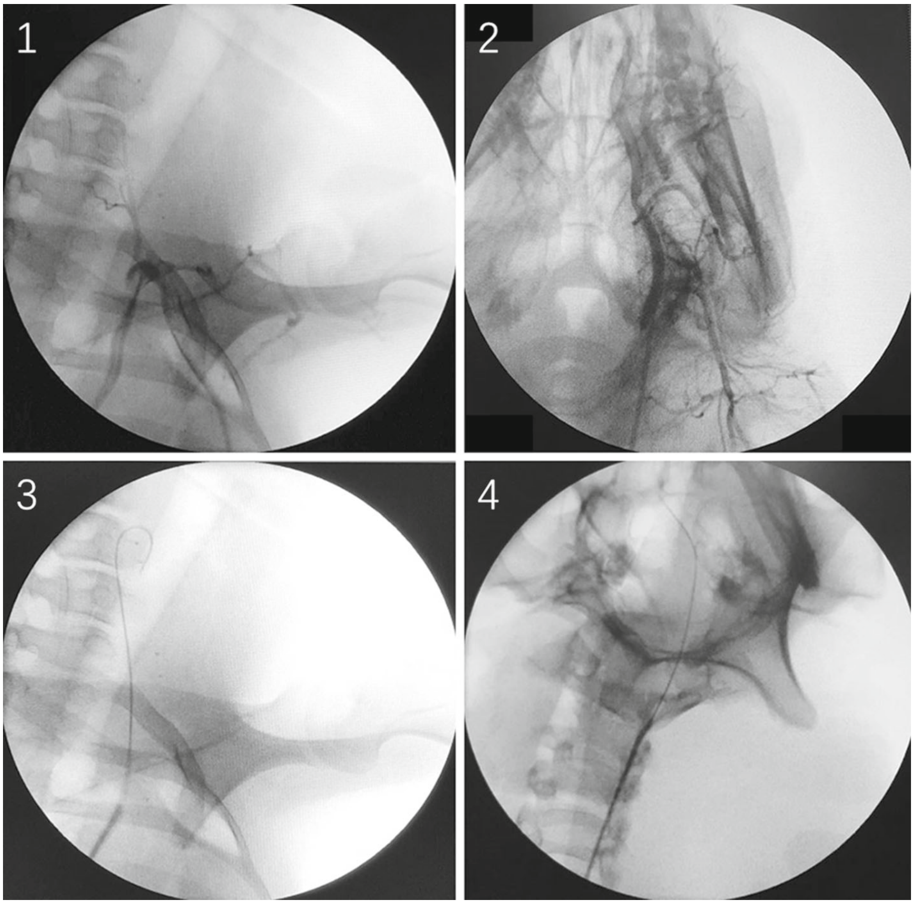

the fluoroscopy images of the angiography, robotic-assisted guidewire insertion, and balloon inflation results, respectively. Moreover, the VI robotic system has now been used for in vivo trials four times. Figure 8(1–4) shows the angiography and guidewire final position results for the second and third in vivo trials, respectively.

Figure 9 compares the surgery and fluoroscopy times of the four in vivo trials. The total time is the time summation of the vascular puncture, guiding catheter insertion, guidewire insertion, and angiography. (The fourth time adds the balloon catheter time.) The absolute error of the total time is hence the error summation of the procedures. The fourth guidewire insertion time includes the automatic and manual control times, along with the automatic balloon catheter insertion time and the guidewire insertion at the key position time. The guidewire insertion at the key position means that we con-

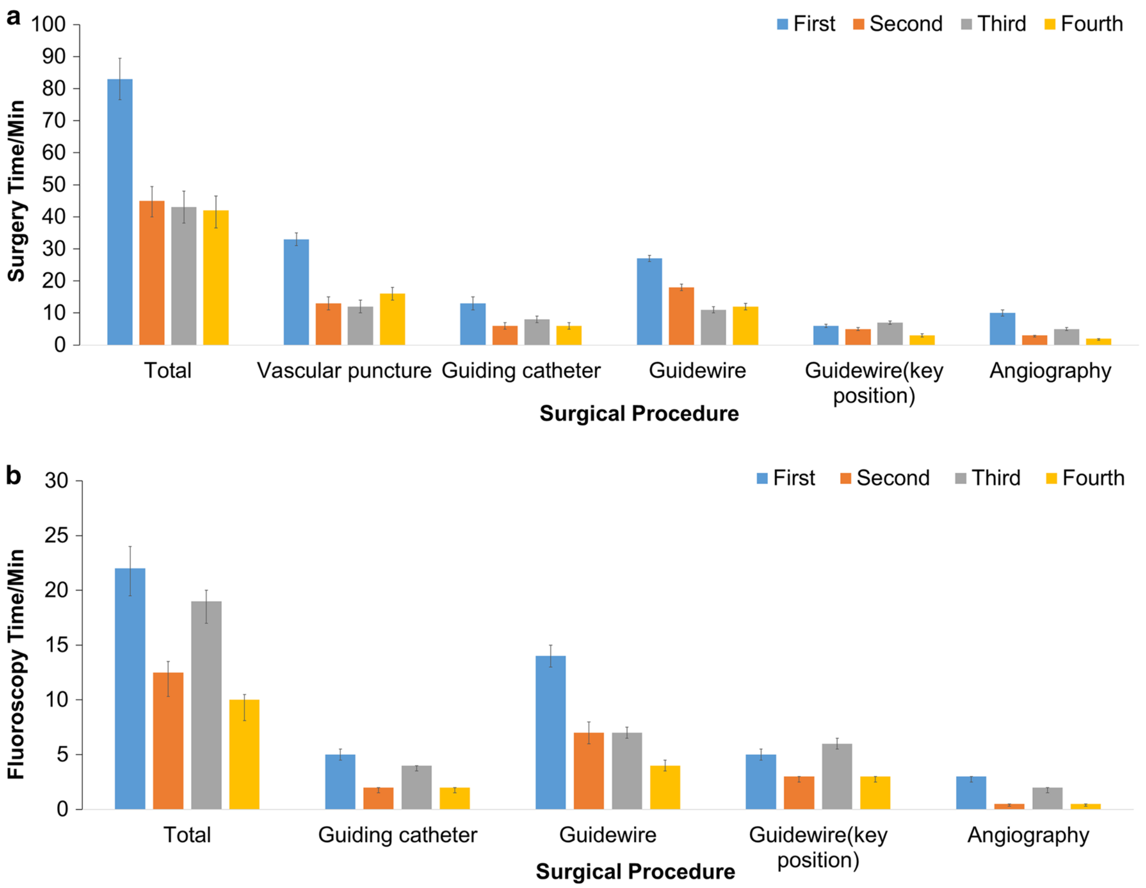

Fig. 9 Surgery time of in vivo trials

trolled the robotic system so as to advance the guidewire tip out of the guiding catheter and into the vascular target. The angiography time adds the additional necessary operations (e.g., extract contrast agent, place the syringe) time, as well as the time to and from the operating room. The fluoroscopy time recorded the duration of the period of X-ray image guidance, which might be longer than the actual fluoroscopy time. In addition, a time less than 0.5 min is calculated as 0.5 min.

We recorded the haptic feedback data (Fig. 10a, b) during the fourth in vivo trial. Based on the analysis of the robotic-assisted procedure and the haptic feedback data, we divided the data into two parts, namely the auto-retract procedure and the operation procedure. As the auto-retract procedure does not allow the surgeon to operate the Omega 3, we eliminated the auto-retract procedure data. Further, the Kalman filter (with a threshold intervention) was used to filter the noisy signals of the operation procedure data (Fig. 10c, d). The initial estimation $\hat{x}_1(F, T) = [0.3, 3.9]$, process noise covariance $Q(F, T) = [1{*}\mathrm{e}{-}4, 1{*}\mathrm{e}{-}4]$, measurement noise covariance $R(F, T) = [4{*}\mathrm{e}{-}2, 4{*}\mathrm{e}{-}2]$, and initial estimation error covariance $\hat{P}_1(F, T) = [1, 1]$, A, B, H are given the unit matrix.

Discussion

From Fig. 6, we can see that the speed and position tracking effects are both really excellent, especially the position tracking. This contributes to the position accuracy of the robotic system. Moreover, from Fig. 6b, c, we can further see that the control model exhibits good robustness and adaptability. However, problems with the assembly, such as a certain non-parallelism and misalignment, affect the speed tracking. Additionally, the high acceleration, low rotational speed, and relatively low sampling frequency result in a bad actual following effect during the acceleration stage, as can be seen in Fig. 6d. In addition, Table 1 presents the position accuracy of the guidewire driving module, which verifies the effectiveness of the control model. The accuracy evaluation results hence fully meet the design requirements.

In the fourth in vivo trial, we successfully accomplished the stent revascularization. In Fig. 7a, the vascular network can clearly be seen, and the angiography result guided the surgeons when performing the robotic-assisted guidewire insertion. From Fig. 7b, c, it can be seen that the guidewire and balloon catheter were placed at the vascular target, and the balloon was successfully inflated. This successful in vivo

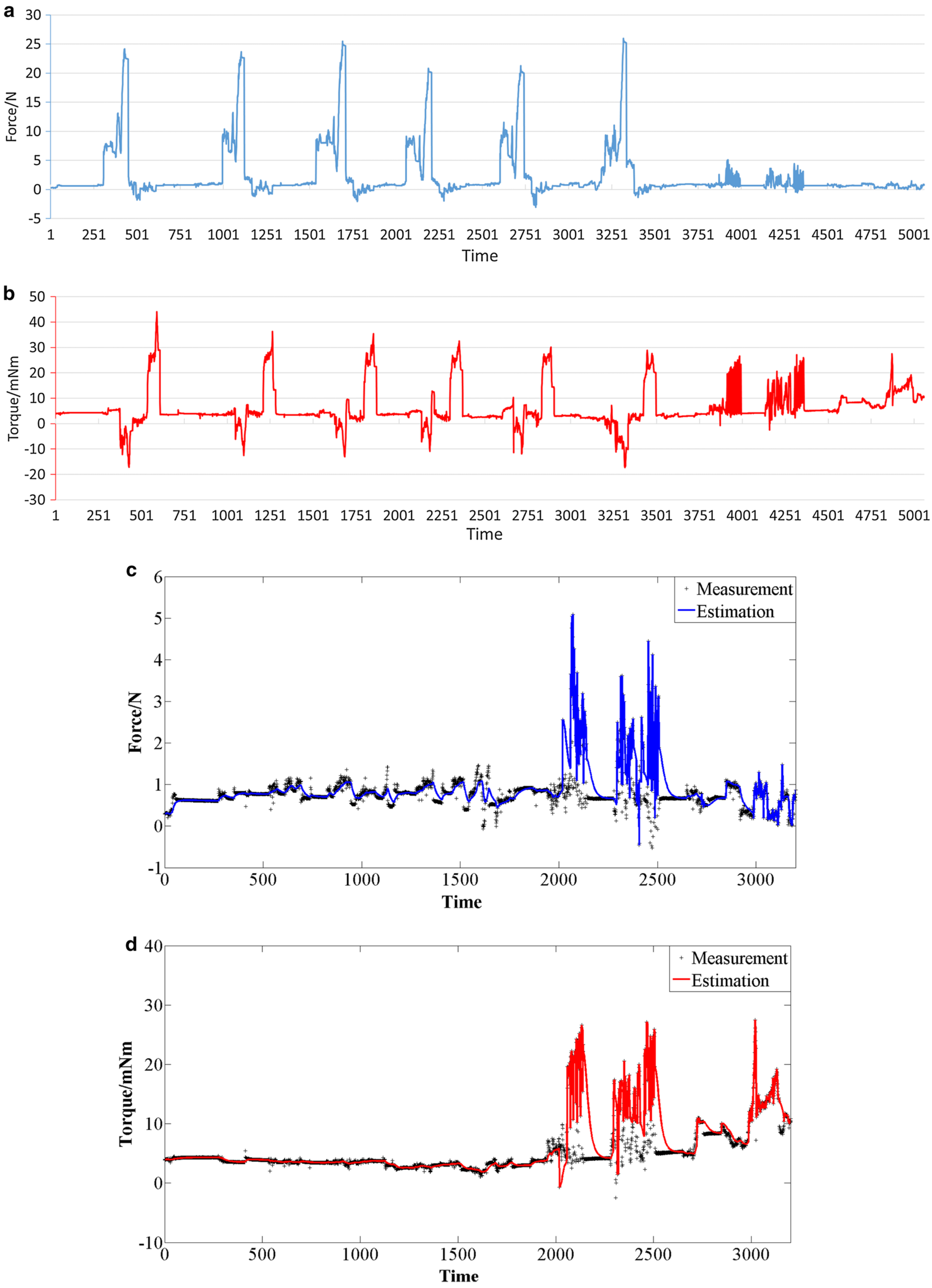

Fig. 10 Haptic feedback data of fourth in vivo trial and Kalman filter results

trial verified the feasibility of our robotic system, which can accomplish important work in the field of VI.

According to Figs. 8(1, 2), 7a and first trial, the angiography results became increasingly clear due to the optimization. Through the four in vivo trials, we identified the injection speed (2 ml/s) and the volume (10 ml) when the angiography was conducted near the arteria carotis. It can be seen that the guidewire was placed at the animal's face as shown in Fig. 8(4). The ultimate aim was to insert the guidewire into the cerebrovascular vessels, so we tried to insert the guidewire into the deep vascular of arteria carotis externa. In addition, we tried to conduct the stent revascularization and advance the balloon catheter. Each trial was a progress, and the robotic system can potentially carry out further study and provide more VI solutions.

From Fig. 9, the total time of the second to fourth in vivo trials was substantially reduced compared with the total time of the first trial, which is owing to the experience of the first trial. For the surgeons, they became familiar with the anatomy of the animal and found the arteria femoralis more quickly than the first trial. This cut lots of time of the vascular puncture. Besides, the surgeons became familiar with the operation of the robotic system. At the second trial, we speeded up the advancement speed, so the guidewire insertion time became shorter. At the third trial, the guidewire insertion in the guiding catheter was manually inserted by the surgeon, so the guidewire insertion time was shorter than the second. However, we inserted the guidewire into the deep vascular of arteria carotis externa, which cost lots of time. And thus, compared with the fourth automatically guidewire insertion time, the third guidewire insertion time was not shorted too much. Besides, fluoroscopy time of the third guidewire insertion was much longer than fluoroscopy time of the second and fourth.

In Fig. 10a, b, there was a clear regularity of the force and torque values. There were periodical peaks and regular fluctuations in the haptic feedback data. This is because of the automatic retracting process. Counterclockwise rotation and the back-clamp fastening are to loosen the chuck, and the force and torque become large until the rotation finishes. Then, the torque becomes small quickly and the shifting board retracts. Finally, clockwise rotation and the back-clamp fastening are to fasten the chuck so that the force continues to increase and the torque increases in reverse. During the in vivo trial, there were several automatic retracting processes, so there were periodical peaks and regularity fluctuation in the haptic feedback data. Of course, these parts of haptic feedback data cannot be felt by the surgeons, so they should be eliminated. Therefore, the Kalman filter was only used for the operation procedure data. Given the violent vibration of the large forces and torques (greater than thresholds), which are the most valuable haptic feedback information for the surgeons, we did not filter the data. As shown in Fig. 10c, d, the high-frequency signals of relatively small forces and torques (less than thresholds) are filtered into the relatively low-frequency signals. Adding the priori (real-time update) and posteriori (real-time measurement) properties, the Kalman filter is potentially suitable for the real-time haptic feedback.

Conclusion

In summary, the four in vivo trials' results of the VI robotic system were satisfying. The surgeons' positive feedback is encouraging for further study of the robotic system. More trials are planned to improve the haptic feedback function.

Acknowledgements This work was supported by High Technology Research and Development Program of China (863 Program, No. 2015AA043203), Natural Science Foundation of China (Nos. 61672341, 61471349), The project of Science and Technology Commission of Shanghai municipality (No. 17441903800), The project of major program of National Natural Science Foundation of China (Nos. 61190124, 61190120), Basic Discipline Layout Project of Shenzhen City (No. JCYJ20150731154850923).

Compliance with ethical standards

Conflict of interest All the authors declare they have no conflict of interest.

Ethical approval The authors declare that all human and animal studies have been approved and performed in accordance with ethical standards.

Informed consent Informed consent was obtained from all individual participants included in the study.

References

1. Venketasubramanian N, Yoon BW, Pandian J, Navarro JC (2017) Stroke epidemiology in south, east, and South-East Asia: a review. J Stroke 19(3):286–294
2. World Health Organization (2017) World health statistics 2017: monitoring health for the SDGs. World Health Organization, Geneva
3. Rafii-Tari H, Payne CJ, Yang GZ (2014) Current and emerging robot-assisted endovascular catheterization technologies: a review. Ann Biomed Eng 42(4):697–715
4. Lin JC (2013) The role of robotic surgical system in the management of vascular disease. Ann Vasc Surg 27(7):976–983
5. Da L, Zhang D, Wang T (2008) Overview of the vascular interventional robot. Int J Med Robot Comp 4(4):289
6. Daneshmand M, Bilici O, Bolotnikova A, Anbarjafari G (2017) Medical robots with potential applications in participatory and opportunistic remote sensing: a review. Robot Auton Syst 95:160–180
7. Arai F, Fujimura R, Fukuda T, Negoro M (2002) New catheter driving method using linear stepping mechanism for intravascular neurosurgery. In: IEEE ICRA, 2002. Proceedings, Vol 3, pp 2944–2949

8. Xiao N, Guo J, Guo S, Tamiya T (2012) A robotic catheter system with real-time force feedback and monitor. Australas Phys Eng Sci Med 35(3):283–289
9. Guo S, Kondo H, Wang J, Guo J, Tamiya T (2007) A new catheter operating system for medical applications. In: IEEE/ICME, pp 82–86
10. Srimathveeravalli G, Kesavadas T, Li X (2010) Design and fabrication of a robotic mechanism for remote steering and positioning of interventional devices. Int J Med Robot Comp 6(2):160–170
11. Aoide N, Hansen, Sensei (2012) Hansen medical. Sensei X robotic catheter system. http://dev-hansen.pantheonsite.io/us/en/cardiacarrhythmia/sensei-robotic-system/product-overview
12. Romo E, Hart SJ, Covington T (2016) Low friction instrument driver interface for robotic systems [P]. US 20160338783 A1
13. Pankratov MM (2011) Robotically assisted PCI with CorPath 200 system: early evidence of potential benefits for patient and physician. Cardiovasc Revasc Med 12(3):e40–e40
14. Pedersen A (2011) Trial to evaluate CorPath robotic system for PCI. Med Device Daily 15(18):1
15. Granada JF, Delgado JA, Uribe MP, Fernandez A, Blanco G, Leon MB, Weisz Giora (2011) First-in-human evaluation of a novel robotic-assisted coronary angioplasty system. JACC-Cardiovasc Interv 4(4):460–465
16. Khan EM, Ng GA, Neelagaru S, Abi-Samra FM, Lee J, Giudici M, Gohn D, Winkle RA, Sussman J, Knight BP, Berman A, Calkins H (2013) First experience with a novel robotic remote catheter system: amigo™ mapping trial. J Interv Card Electr 37(2):121–129
17. Won JY, Yi BJ, Cha HJ (2016) Review of new master/slave catheter driving vascular intervention robot system: intervention radiologist's perspective. HMR 36(4):225
18. Shen H, Wang C, Xie L, Zhou S, Gu L, Xie H (2018) A novel remote-controlled robotic system for cerebrovascular intervention. Int J Med Robot Comput Assist Surg Mrcas, 14: e1943
19. Zeng Q, Zhou SJ, Shen H, Wang C (2018). A network communication protocols for robotic-assisted vascular intervention systems. BST
20. Li Zi-Yan, Jing-Li Fu, Chen Li-Qun (2009) Euler–lagrange equation from nonlocal-in-time kinetic energy of nonconservative system. Phys Lett A 374(2):106–109
21. Bai Z (2004) Study of a 3-dof parallel manipulator dynamics based on lagrange's equation. J B Univ Aeronaut Astronaut 30(1):51–54
22. Xia HY, Zhan WB (2003) Application and development expression of lagrange equation. J Luoyang Teach Coll 2:27–29
23. Edwards C, Spurgeon S (1998) Sliding mode control: theory and applications. CRC Press, Boca Raton
24. Utkin VI, Chang HC (2007) Sliding mode control on electro-mechanical systems. Math Probl Eng 8(4–5):451–473
25. Liu J, Wang X (2011) Advanced sliding mode control for mechanical systems. Tsinghua University Press, Springer, Berlin
26. Liu J (2013) Radial basis function (rbf) neural network control for mechanical systems. Springer, Berlin, pp 19–53
27. Seshagiri S, Khalil HK (2000) Output feedback control of nonlinear systems using RBF neural networks. In: Proceedings of the ACC, 1999, Vol 11, pp 2808–2812
28. Welch G, Bishop G (1995). An introduction to the kalman filter. Course Notes 8 of ACM SIGGRAPH 2001, 8(7): 127–132
29. Evensen G (2003) The ensemble kalman filter: theoretical formulation and practical implementation. Ocean Dyn 53(4):343–367
30. Brown RG, Hwang PYC (1997) Introduction to random signals and applied Kalman filtering: with MATLAB exercises and solutions. Wiley, New York
31. Ovando-Shelley E, Santoyo E, de Oliveir M (2013) Intervention techniques. Geotechnical engineering for the preservation of monuments and historic sites, pp 75–91